Theory of nondegenerate-spectrum reversal and its breaking

Chenji Gu,* Boaz Ilan, and Jay E. Sharping
School of Natural Sciences, University of California–Merced, Merced, California 95343, USA
(Received 27 August 2013; published 25 October 2013)

We theoretically study spectrum reversal and spectral-temporal similarity-and-inversion phenomena in nondegenerate four-wave mixing of ultrashort optical pulses. The key ingredients leading to spectrum reversal between two waves are identified, showing that energy conservation alone is insufficient. Only under certain conditions can the shapes of the two waves in the time and frequency domains possess special relations. Specifically, the two waves can have nearly identical temporal shapes, whereas their spectral shapes are reversed. In addition, the temporal and spectral shapes are the same for one wave and reversed for the other. However, non-negligible parasitic effects in ultrafast dynamics can breakup these relationships under more general conditions. The physical mechanisms underlying these phenomena are explored analytically and confirmed by direct numerical computations of the governing equations.

DOI: 10.1103/PhysRevA.88.043839 PACS number(s): 42.65.Sf, 42.65.Re, 42.79.Nv

I. INTRODUCTION

Special relationships between time and frequency reveal a deeper understanding of physical systems and can lead to better ways to control them. In this vein, the authors have recently demonstrated "spectral mirror imaging" (SMI), a phenomenon in which two ultrashort optical pulses possess oppositely shaped spectra [1]. SMI occurs when the pulses overlap spatially and temporally while undergoing a nondegenerate four-wave-mixing (FWM) process. Thus far, the origin of SMI has not been studied in detail.

In this study we explore the physical origin of SMI. Intuitively, one might expect that SMI follows from energy conservation. However, we show that the condition of energy conservation alone is insufficient to deduce SMI. In fact, due to non-negligible parasitic effects present in ultrafast pulse propagation, the two waves do not generally feature oppositely shaped spectra. We find that only under certain conditions are the spectral shapes of two waves reversed with respect to the center frequency of the controlling pump pulse. In addition, we identify a relationship between the temporal and spectral amplitude shapes, i.e., one wave exhibits shape similarity in the time and frequency domains, while the other wave exhibits temporal and spectral shapes that are reversed with respect to one another. We call this phenomenon "spectral-temporal similarity and inversion" (STSI).

We present an analytic theory for these two special relationships. The key physical mechanisms and operating conditions responsible for SMI are opposite values of group-velocity dispersion (GVD) for the two waves and their complex-conjugated parametric gain. The conditions leading to STSI are large GVD and a strong initial chirp. The physical mechanisms underlying SMI and STSI are explored analytically and confirmed by direct numerical computations of the governing system of nonlinear Schrödinger (NLS) equations.

The interrelationships between temporal and spectral properties of waves offer physical insights into ultrafast phenomena that have application to state-of-the-art spectroscopic and imaging techniques of ultrafast processes. These interrelationships are applicable to other nonlinear wave systems as well.

II. FUNDAMENTALS OF SMI THROUGH ULTRAFAST FWM PROCESSES

In this section, we briefly review the previous related work, starting with the general concept of phase conjugation in the time domain and its relation to SMI. We present a common, yet incorrect, argument according to which SMI follows from energy conservation in FWM processes. We also highlight the key role of NLS equations in modeling the dynamics of ultrafast FWM processes. These equations are at the focus of the analytical and computational modeling in this study.

A. SMI as a concept and physical model

The special relationships of interest are illustrated in Fig. 1. This figure depicts how SMI is closely related to another concept, that of temporal phase conjugation (TPC, also known as midspan spectral inversion in optical communications). To represent and understand the connections between TPC and SMI fundamentally, consider the complex electric fields of two optical pulses, called "wave 1" and "wave 2", that are copropagating along the z direction with electric fields

$$E_n(t,z) = A_n(t,z)e^{-i(kz-\omega_n t)}, \quad n = 1,2, \tag{1}$$

where $A_n(t,z)$ is a slowly varying complex envelope and the fast carrier of "wave n" is centered at frequency ω_n. The spectrum of each pulse centered at its own reference frequency is

$$\hat{A}_n(\omega,z) = \int A_n(t,z)e^{-i\omega t}\,dt = \hat{E}_n(\omega+\omega_n,z). \tag{2}$$

As depicted on the top of Fig. 1, TPC signifies that the temporal phase profiles of two pulses are inverted, i.e.,

$$\arg\{A_2(t,z)\} = \varphi_0 - \arg\{A_1(t,z)\}, \tag{3}$$

where φ_0 is a constant absolute phase. When the amplitudes of two pulses are the same, this condition is equivalent to

$$A_2(t,z) = e^{i\varphi_0}A_1^*(t,z). \tag{4}$$

*cgu2@ucmerced.edu

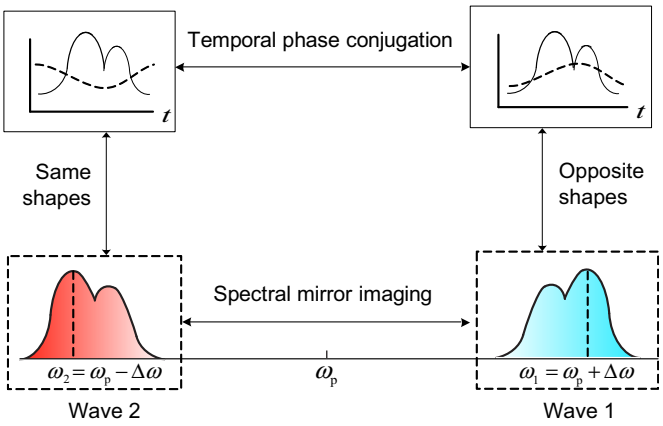

FIG. 1. (Color online) Illustration of special relationships between two waves in the time (top) and frequency (bottom) domains. Horizontally, the connection between two waves is featured as SMI. Vertically, whereas "wave 2" exhibits similarity between its temporal and spectral shapes, "wave 1" has opposite temporal and spectral shapes.

Taking the Fourier transform of the general TPC relation (4) gives

$$\hat{A}_2(\omega,z) = e^{i\varphi_0}\hat{A}_1^*(-\omega,z), \tag{5}$$

and taking the absolute values yields

$$|\hat{A}_2(\omega,z)| = |\hat{A}_1(-\omega,z)|. \tag{6}$$

This relation manifests SMI, i.e., in the frequency domain the shapes of the spectral amplitudes of the two waves appear as mirror images of each other with respect to a center frequency as depicted on the bottom of Fig. 1.

Earlier studies of TPC can be traced back two decades ago when this concept was used to compensate for pulse broadening due to chromatic dispersion in optical fibers [2,3]. On the other hand, SMI, which is the spectral counterpart of TPC, has only recently been studied and demonstrated through ultrafast FWM [1]. Detailed characterization of ultrashort pulses can be difficult to achieve due to the need for sophisticated diagnostic techniques (cf. [4,5]). The vast majority of previous reports on spectrum reversal are wavelength-shift-free [6,7] based on narrowband light sources.

One might suspect that SMI should always occur due to energy conservation. This argument typically goes as follows. Consider a conservative interaction of an intense optical "pump" field with a nonlinear medium, in which two incident pump photons are annihilated and two new photons are created, as happens in a FWM process [8]. Since the energy of a photon is proportional to its frequency, $E = \hbar\omega$, the pump frequency is twice the sum of the frequencies of the two new photons due to energy conservation, i.e.,

$$2\omega_p = \omega_1 + \omega_2. \tag{7}$$

As pump photons are annihilated and replaced with new ones, two continuous sidebands arise and their amplitudes are the same. Then one might figuratively "expand" the amplitudes at each frequency and conclude from the relation (7) that the two sidebands should always appear as mirror images with respect to the pump frequency.

However, the argument above is *incorrect* in the last step of speculation. Formally speaking, the analysis above only applies to FWM process for monochromatic waves or the center frequencies of two spectral sidebands. In the ultrafast regime, this generalization of amplitudes (spectral shapes) from a series of single frequencies fails. This failure is demonstrated in Sec. IV B, where the spectral shapes are not reversed, in spite of the fact that the system is conservative and the two waves have the same energy. This means that for ultrashort pulses with broadband spectra, a FWM process does not necessarily lead to two waves whose spectra are the opposite shape. To obtain a quantitative theory which reveals detailed information about the spectral shape, one must perform careful simulations of the ultrafast FWM process using coupled NLS equations [1].

Additionally, narrowband light sources produce continuous-wave or long pulse durations. Broadband light sources deliver ultrashort pulse durations, typically in the femtosecond or picosecond regimes. The concepts of spectral shape and temporal phase have little meaning when referring to narrowband, long pulse, or continuous-wave light sources. In short, in order to theoretically explore SMI one must perform the computation of coupled NLS equations. Experimentally, this means one should use ultrashort pulses with broadband spectra [1] instead of continuous-wave or long pulse light sources with narrowband spectra [6,7].

B. Equations for ultrafast FWM processes

Motivated by the need for a deeper understanding of our recent experimental observation of SMI [1], we consider the propagation of ultrashort optical pulses through a FWM process. The wave dynamics in lossless media can then be modeled by three coupled NLS equations for the pump field, A_p, and the two sideband waves A_1, A_2, as (cf. [9])

$$i\frac{\partial A_p}{\partial z} - \frac{1}{2}\beta_{2,p}\frac{\partial^2 A_p}{\partial t^2} + \gamma[|A_p|^2 + 2|A_1|^2 + 2|A_2|^2]A_p - 2\gamma A_1 A_2 A_p^* e^{i\Delta\beta_{\rm lin} z} = 0, \tag{8a}$$

$$i\frac{\partial A_n}{\partial z} + i\Delta\beta_{1,n}\frac{\partial A_n}{\partial t} - \frac{1}{2}\beta_{2,n}\frac{\partial^2 A_n}{\partial t^2} + \gamma[2|A_p|^2 + 2|A_{3-n}|^2 + |A_n|^2]A_n - \gamma A_p^2 A_{3-n}^* e^{-i\Delta\beta_{\rm lin} z} = 0, \tag{8b}$$

where the last equation represents two equations ($n = 1,2$). Let us recap the physical meaning of each of the terms and coefficients. γ is the nonlinear coefficient of the medium is and $\beta_{2,n}$ are the GVDs of "wave n". The difference between the group velocities of the pump and "wave n" is $\Delta\beta_{1,n} = \beta_1(\omega_n) - \beta_1(\omega_p)$. The *linear phase mismatch* coefficient in the exponents is

$$\Delta\beta_{\rm lin} = \beta(\omega_1) + \beta(\omega_2) - 2\beta(\omega_p). \tag{9}$$

In Eq. (8b), the second term represents the walk-off between the pump and wave n. The third term represents dispersive wave propagation from the contribution of GVD. The fourth term represents self-phase modulation of wave n, and cross-phase modulation (XPM) induced the combined effects of the pump and the other "wave $(3-n)$". The fifth term represents energy flow among the three waves. The direction

and magnitude of energy flow are governed by the phase-mismatched coefficient $\Delta\beta_{\rm lin}$.

Unfortunately, there is no closed-form general solution for system (8). However, this system is amenable to direct computations.

III. ANALYTIC THEORY OF SMI

Under some basic assumptions, the nonlinear system (8) can be simplified into two linearly coupled-wave equations and solved analytically. In this way, we obtain special solutions that exhibit SMI, allowing us to obverse the physical mechanisms underlying this phenomenon.

A. Coupled-wave equations and special solutions with SMI features

As we mentioned above, an accurate modeling of the temporal and spectral dynamics requires solving system (8) numerically. To gain insight into this dynamics, it is expedient to begin with a simpler approach by making the undepleted pump approximation. This allows us to capture some of the major aspects of SMI. For the moment, we simply consider the following linearly coupled system of two equations:

$$i\frac{\partial A_1}{\partial z}-\frac{1}{2}\beta_{2,1}\frac{\partial^2 A_1}{\partial t^2}=\frac{1}{L_{\rm nl}}A_2^*, \tag{10a}$$

$$i\frac{\partial A_2}{\partial z}-\frac{1}{2}\beta_{2,2}\frac{\partial^2 A_2}{\partial t^2}=\frac{1}{L_{\rm nl}}A_1^*, \tag{10b}$$

where $L_{\rm nl}$ is a characteristic nonlinear length [see (14) below for details].

Strictly speaking, system (10) is a linear one—it is as though the two waves copropagate in a *linear* dispersive system. However, the nonlinear effects present in system (8) are "hidden" in the form of parametric gain, i.e., the terms on the right-hand sides of (10). Parametric gain is inherent in FWM (and other nonlinear-wave-mixing processes, cf. [8]). Note that the terms with parametric gain have the complex conjugation of the fields, i.e., the amplification of one wave proportional to the complex conjugate of the other. This *conjugated gain* is one of the key requirements for SMI.

Furthermore, for dispersive wave propagation one may assume that two waves experience *opposite GVDs*, i.e.,

$$\beta_{2,1}=-\beta_{2,2}\equiv-\beta_2. \tag{11}$$

This is another key requirement for the special relations that follow. The opposite GVDs produce one wave with a blueshifted spectrum and the other wave with a redshifted spectrum. Justification of this assumption is discussed in Appendix A.

In the femtosecond domain, both mechanisms, namely conjugated gain and opposite GVDs, contribute to SMI. When the pulses become longer, i.e., in the picosecond domain, the contribution from the GVD plays a minor role in SMI. This is confirmed by our computation results in Sec. IV A.

Before discussing the analytic solution of system (10), it is easy to verify that the coupled equations (10) with condition (11) admit solutions that satisfy the following *self-consistent* relations:

$$A_2(t,z)=\pm iA_1^*(t,z). \tag{12}$$

Relations (12) manifest two special cases of TPC relation (4). To incorporate the effect of phase mismatch, it is expedient to present a more general system of two coupled linear Schrödinger equations,

$$i\frac{\partial A_1}{\partial z}+\frac{1}{2}\beta_2\frac{\partial^2 A_1}{\partial t^2}=\frac{e^{-i\Delta\beta_{\rm lin}z}}{L_{\rm nl}}A_2^*, \tag{13a}$$

$$i\frac{\partial A_2}{\partial z}-\frac{1}{2}\beta_2\frac{\partial^2 A_2}{\partial t^2}=\frac{e^{-i\Delta\beta_{\rm lin}z}}{L_{\rm nl}}A_1^*. \tag{13b}$$

In Appendix A, under the assumption of a long pulsed strong undepleted pump wave, we derive the linear system (13) from the nonlinear system (8). In doing so, the characteristic nonlinear length is found to be

$$L_{\rm nl}\doteq\frac{1}{\gamma P_0}, \tag{14}$$

where P_0 is the peak power of pump.

Comparing systems (13) and (8b), the third and fifth terms in Eq. (8b) are present in both systems. However, the second and fourth terms in (8b) are missing. Thus, system (13) only considers the contribution from dispersive wave propagation and parametric gain with phase mismatch. We show later that this approach captures the major physical mechanisms of SMI, yet it omits some subtleties that can actually make the SMI feature more distinguishable.

In Appendix B we prove that system (13) admits special solutions that satisfy the SMI relation (5). More precisely, we prove that system (13) admits SMI *if, and only if,* the input waves satisfy one of the two SMI conditions,

$$\hat{A}_2^*(-\omega,0)=\pm r_-\hat{A}_1(\omega,0), \tag{15}$$

where r_- is a complex number of unit magnitude [see Eq. (B6) and subsequent analysis]. Physically, relations (15) mean that two waves are required to be conjugated (up to a constant phase) at the input.

To recap, SMI and TPC can arise as special solutions for two copropagating waves in a linear dispersive system, in which the two waves experience opposite GVDs and conjugated gain.

B. Discussions on asymptotic solutions with SMI feature

As proved in Appendix B, system (13) admits an asymptotic solution exhibiting SMI, even without the requirement of a conjugated wave as the input. This asymptotic solution suggests that SMI should always hold for large propagation distances. However, recall that this analysis is based on system (13), which is a simplification of system (8).

As we mentioned above, by comparing the format of two Eqs. (13) and (8b), one can identify that the similar format of the third and fifth terms in Eq. (8b) is preserved, while the second and fourth terms are missing. Thus system (13) only considers the contribution from dispersive wave propagation and parametric gain with phase mismatch. However, system (13) neglects the contribution from walk-off and the important fact that the pump wave is also an ultrashort pulse. As we will show in the next section, these effects can distort the spectrum of each sideband wave in the frequency domain.

One might consider these effects "parasitic". However, for the practical consideration of ultrafast FWM processes (broadband spectra with widely separated wavelength difference), the dispersion and walk-off are persistent. To fully appreciate their significance, in the next section we solve the nonlinear system (8).

IV. COMPUTATIONAL STUDIES ON SMI

In this section, we focus on computational modeling of the nonlinear system (8). To solve this system we use standard numerical techniques for ultrashort pulse propagation, i.e., the split-step Fourier transform method [10]. The purpose of these computations is not only to find SMI, but also to identify under which conditions it arises. In particular, we show that parasitic effects can "break" SMI, even though system (8) conserves the total energy and the energies of the two sideband waves are the same.

The input (initial conditions) for the nonlinear system (8) is specified for the pump and the two waves (corresponding to the two sidebands). The input pump wave is assumed to be real-valued ("transform-limited") and temporally delayed with respect to the two waves. The input for "wave 1" is taken to have a sech profile (a Gaussian profile would lead to similar results). For the moment, we do not specify the input for "wave 2"—it is absent (zero) in certain simulations below, which mimics the pump-probe technique. Thus, the input pump and wave 1 are

$$A_p(t,0) = \sqrt{P_0}e^{-\frac{(t+\tau)^2}{2T_0^2}}, \tag{16a}$$

$$A_1(t,0) = \sqrt{P_1}\,\mathrm{sech}\left(\frac{t}{T_1}\right)e^{-\frac{iCt^2}{T_1^2}}, \tag{16b}$$

where P_0 and P_1 are peak powers, T_0 and T_1 are pulse durations, C is (dimensionless) chirp, and τ is the initial time delay between the pump and two waves (the waves are ahead of the pump when $\tau < 0$). In the picosecond regime, we use $T_0 = 8$ ps, $P_0 = 780$ W, $T_1 = 2$ ps, $P_1 = 0.04$ W, and the fiber length is $L = 1.2$ m. In the femtosecond regime, we use $T_0 = 400$ fs, $P_0 = 30$ kW, $T_1 = 10$ fs, $P_1 = 4$ W, and the fiber length is $L = 3$ cm.

The physical parameters inside of nonlinear system (8) used in these computations are chosen corresponding to two experiments which have different pulse-width regimes: (i) the picosecond regime (see [11]), and (ii) the femtosecond regime (see [12]). In all cases, $\gamma = 11$ $(\mathrm{W\,km})^{-1}$. The dispersion parameters in the picosecond regime are $\Delta\beta_{1,1} = 0.864$ ps/m, $\Delta\beta_{1,2} = 0.821$ ps/m, $\beta_{2,p} = -0.470$ ps^2/km, $\beta_{2,1} = -12.9$ ps^2/km, $\beta_{2,2} = 13.8$ ps^2/km, and $\Delta\beta_{\mathrm{lin}} = -13.2$ m^{-1} The dispersion parameters in the femtosecond regime are $\Delta\beta_{1,1} = 1.73$ ps/m, $\Delta\beta_{1,2} = 1.56$ ps/m, $\beta_{2,p} = -0.621$ ps^2/km, $\beta_{2,1} = -23.5$ ps^2/km, $\beta_{2,2} = 28.2$ ps^2/km, and $\Delta\beta_{\mathrm{lin}} = -38.2$ m^{-1}.

We decompose the temporal and spectral outputs of the two sideband waves after a propagation distance $z = L$ as

$$A_n(t,L;\tau) = \Psi_n(t;\tau)e^{i\Phi_n(t;\tau)}, \quad n = 1,2, \tag{17a}$$

$$\hat{A}_n(\omega,L;\tau) = \hat{\Psi}_n(\omega;\tau)e^{i\hat{\Phi}_n(\omega;\tau)}, \quad n = 1,2, \tag{17b}$$

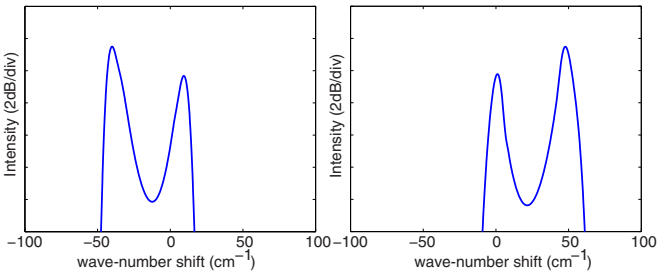

FIG. 2. (Color online) Spectral shapes of two waves when $\tau = 3$ ps.

where τ is the initial delay we already defined in (16a), Ψ is the temporal amplitude, Φ is the temporal phase, $\hat{\Psi}$ is the spectral amplitude, and $\hat{\Phi}$ is the spectral phase.

A. Spectrum reversal: Conjugated inputs

As the first series of computations, the two input waves are assumed to be initially conjugated,

$$A_2(t,0) = iA_1^*(t,0). \tag{18}$$

The computational results shown in Fig. 2 depict the spectral shapes of the two waves in the picosecond regime, for a specific value of the initial delay τ. The left and right profiles depict the spectra of "wave 2" and "wave 1", respectively. It is clear that two waves are mirror images of one another in the frequency domain.

To present the SMI feature more clearly, we also show the spectra $|\hat{A}_n(\omega,L;\tau)| = \hat{\Psi}_n(\omega;\tau)$ as a function of τ, i.e., the spectrograms of two waves. The left and right columns in Figs. 3 and 4 correspond to the spectrograms of "wave 2" and "wave 1", respectively.

In the picosecond regime, spectrograms appear as mirror images of each other—whether the input waves are chirped [top plots shown in Fig. 3(a)] or unchirped [bottom plots shown in Fig. 3(b)]. These spectrograms shows lumps, which

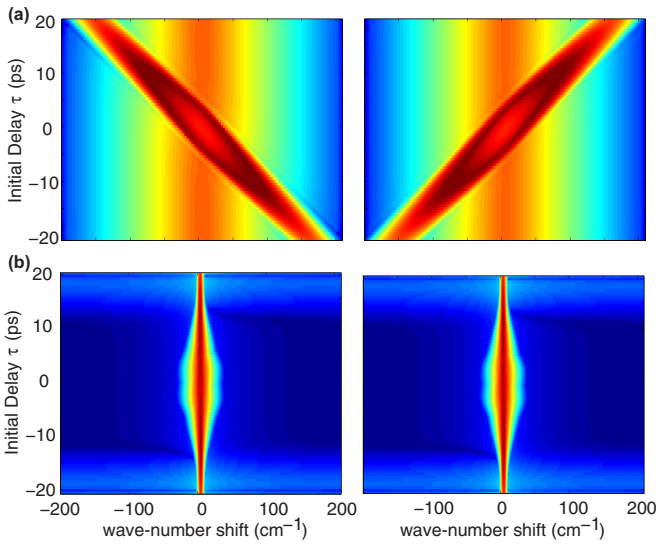

FIG. 3. (Color online) Demonstration of SMI through system (8) in the picosecond regime using conjugated input waves with (a) input chirp $C = -20$; (b) unchirped input waves ($C = 0$).

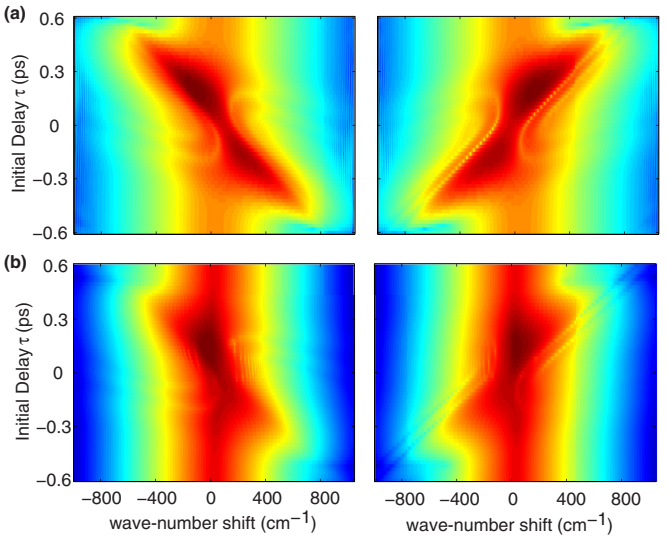

FIG. 4. (Color online) Demonstration of SMI through system (8) in the femtosecond regime using conjugated input waves with (a) input chirp $C = -1$; (b) unchirped input waves ($C = 0$).

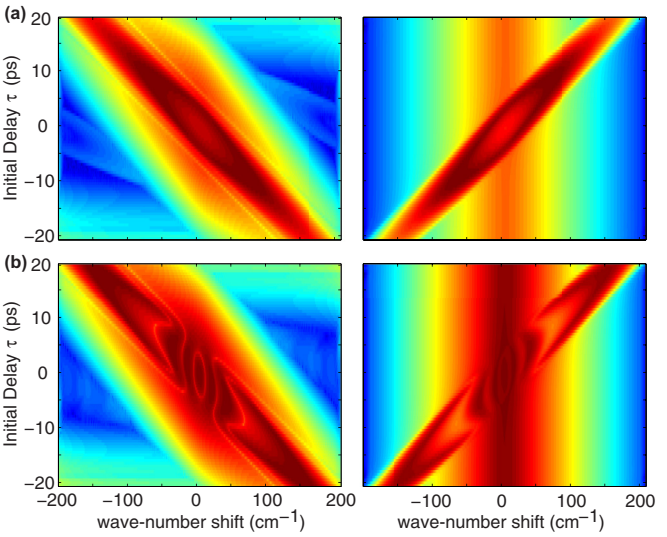

FIG. 5. (Color online) Degradation of SMI through system (8) in the picosecond regime using nonconjugated input waves. Initial conditions are $A_2 = 0$, and A_1 is with chirp $C = -20$ and peak power (a) $P_1 = 0.04$ W; (b) $P_1 = 400$ W.

correspond to the higher-intensity spectral amplitude. Thus, *system (8) with conjugated input waves exhibits the feature of SMI*. However, there is an important distinction due to the chirp. When the input waves are chirped, these lumps are *oblique* and possess inverse slopes (approximately at $\pm 45^\circ$), which makes SMI easily *distinguishable*. On the other hand, when the input waves are unchirped, these lumps are vertical, i.e., each sideband spectrum itself is symmetric with respect to its center frequency. In such cases, though the waves do exhibit SMI, this might not be evident by comparing their spectra.

A similar picture arises in the femtosecond regime (Fig. 4), though SMI is not as sharp as in the picosecond regime due to the broader spectra. However, in the femtosecond case, one can observe a distinguishable SMI feature no matter whether the initial chirp is added [as shown in Fig. 4(a)] or not [as shown in Fig. 4(b)].

To summarize the above computational results in the two different pulse-width regimes, when using conjugated waves at the input, an input chirp is required to observe the distinguishable SMI feature in the picosecond regime, but such a chirp is not required in the femtosecond regime.

B. Breaking spectrum reversal: Nonconjugated inputs

As the second series of computations, the input two waves are assumed to be not initially conjugated. Specifically, "wave 2" is absent at the input, i.e.,

$$A_2(t,0) = 0. \tag{19}$$

Everything else is the same as in the computations above. This initial condition is used to emulate the common approach in the pump-probe technique.

Figures 5(a) and 6(a) (top plots) show the spectrograms of the two waves. Clearly, the SMI features in these computations are degraded compared with the results in Sec. IV A. The spectrograms of "wave 1" possess an additional vertical lump, which is not mirrored in "wave 2". Moreover, comparing Figs. 5(b) and 6(b) (bottom plots), as the peak power of wave 1 is increased, the distortion between the shapes of the two sidebands becomes more evident. Hence, despite the fact that two waves have the same energy, "wave 2" does not become the mirror image of "wave 1".

It is interesting to remark that other theoretical studies have suggested that the relationship of spectrum reversal can be destroyed; cf. [13]. Our computational results of system (8) with nonconjugated waves at the input show this in detail. These counterexamples prove that energy conservation in ultrafast FWM processes *is not* sufficient to give rise to SMI. As long as the two waves have equal energies, the distributions of spectral intensities can be quite arbitrary.

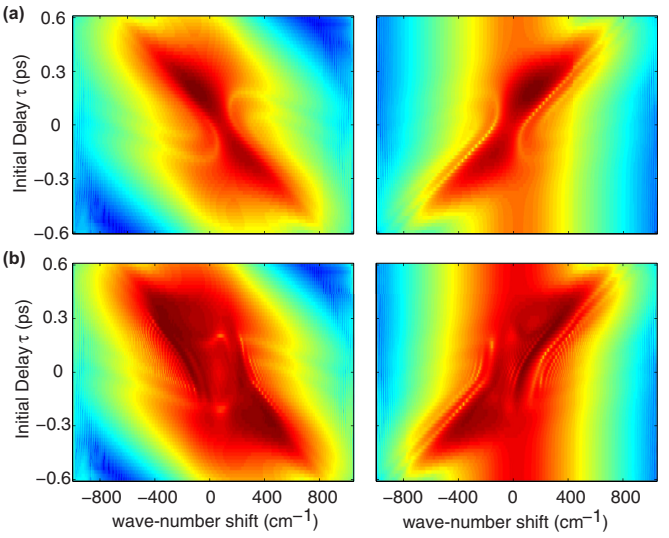

FIG. 6. (Color online) Degradation of SMI through system (8) in the femtosecond regime using nonconjugated input waves. Initial conditions are $A_2 = 0$, and A_1 is with chirp $C = -1$ and peak power (a) $P_1 = 4$ W; (b) $P_1 = 10$ kW.

C. Analysis of distinguishable SMI features

Recall that the asymptotic solutions of system (13) predict that SMI should always occur for long propagation distance, even when the input waves are not conjugated. However, the analysis in Appendix B neglects the effects of walk-off during the pulse propagation due to material dispersion. The computational results based on system (8) show that the effect of walk-off can either "enhance" or "obscure" SMI. On the one hand, the effect of walk-off in combination with either input chirp or GVD (distributed chirp) can distort the profile of each sideband and break the SMI feature, as can be seen, for example, comparing the results in Figs. 3 and 5 (or Figs. 4 and 6). On the other hand, when the inputs are conjugated, the combined contributions of walk-off and chirp make the SMI feature more distinguishable, because the profile of each sideband is highly asymmetric, as can be seen, for example, comparing the results in Figs. 3(a) and 3(b). We remark that the condition of conjugated waves as input excludes the commonly used pump-probe approach, in which the other sideband is absent at the input.

To understand why the input chirp is also essential for distinguishing SMI, first consider an unchirped (real-valued) wave that is inhomogeneously amplified in the time domain by the pump wave due to the effect of walk-off. Since the amplitude of a real-valued function's Fourier transform is always symmetric, the amplitudes of the spectral sidebands must be symmetric as well. However, when the wave is chirped and inhomogeneously amplified in the time domain, the spectrum will generally be asymmetric.

V. SPECTRAL-TEMPORAL SIMILARITY AND INVERSION

In this section, we identify and investigate a different yet related temporal-spectral feature in a nondegenerate FWM process. Specifically, when two ultrashort pulses overlap spatially and temporally, under certain conditions found below, one wave exhibits shape similarity in the time and frequency domains, while the other wave exhibits temporal and spectral shapes that are reversed with respect to one another. We call this phenomenon spectral-temporal similarity and inversion (STSI), vertically depicted in Fig. 1. Actually, SMI and STSI, can—and typically do—occur in tandem. When referring to SMI, the focus is on the comparison of two different waves in the frequency domain. When referring to STSI, the focus is on the comparison of the spectral and temporal properties of the same wave. We also investigate the physical mechanisms underlying STSI computationally and analytically, based on the same models presented in Sec. II B.

A. Computational studies on STSI

Here we present computational results of STSI. Our computations use the same assumptions in Sec. IV A, i.e., conjugated waves as the input, for two waves in the femtosecond and picosecond regimes. In the figures below, the left (right) panel depicts the temporal (spectral) amplitude and chirp of each wave [see Eqs. (17) for these decompositions].

In the picosecond regime, all the parameters in our computations are the same as in Fig. 2, except that the input power has been increased to $P_1 = 25$ W. Figures 7 and 8 show the outputs for "wave 2" and "wave 1", respectively.

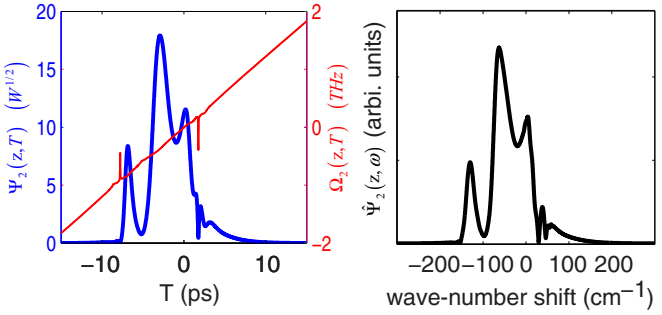

FIG. 7. (Color online) Spectral-temporal similarity for "wave 2" in the picosecond regime.

In the femtosecond regime, all the parameters in our computations are the same as in Fig. 4, except that $P_1 = 100$ W and the input delay is $\tau = 5$ fs. Figures 9 and 10 show the outputs for "wave 2" and "wave 1", respectively.

From the results above, we observe that "wave 2" (Figs. 7 and 9) exhibits identical or similar shapes, in both the picosecond and femtosecond regimes. On the other hand, "wave 1" (Figs. 8 and 10) exhibits reversed shapes, in both the picosecond and femtosecond regimes. In other words, these results show that, within one nonlinear system, two sideband waves exhibit STSI features.

B. Analytic theory of STSI

Our computational results show that STSI occurs in ultrafast FWM processes. To obtain more physical insight into this phenomenon, we reconsider the simplified linear system (13). In Appendix B we derive the special solutions of this system exhibiting the feature of SMI. Recapitulating Eq. (B14),

$$\hat{A}_1(\omega,z) = e^{\frac{1}{2}i(\beta_2\omega^2-\Delta\beta_{\rm lin})z}e^{\gamma P_0\Gamma z}\hat{A}_1(\omega,0).$$

Applying the inverse Fourier transform gives

$$A_1(t,z) = e^{-\frac{1}{2}i\Delta\beta_{\rm lin}z}e^{\gamma P_0 z}\frac{1}{2\pi}\int e^{\frac{1}{2}i\beta_2\omega'^2 z}e^{i\omega' t}\hat{A}_1(\omega',0)\,d\omega'. \tag{20}$$

Let the characteristic temporal duration of the input wave be T, which is inversely proportional to its characteristic bandwidth. For an ultrashort pulse that propagates a distance z, the pulse duration is much smaller than the characteristic

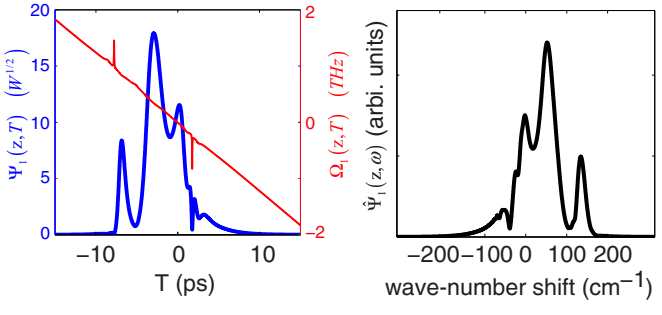

FIG. 8. (Color online) Spectral-temporal inversion for "wave 1" in the picosecond regime.

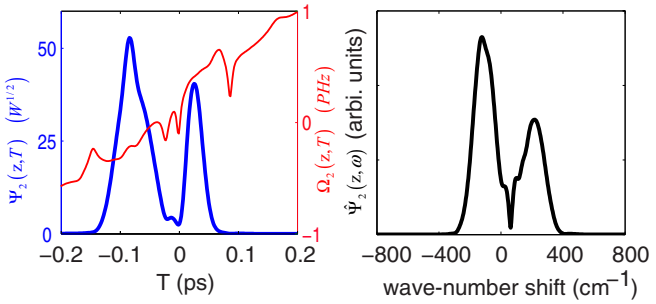

FIG. 9. (Color online) Spectral-temporal similarity for "wave 2" in the femtosecond regime.

dispersion length, i.e.,

$$\frac{|\beta_2 z|}{T^2} \gg 1. \tag{21}$$

Therefore, the phase in the complex exponent in Eq. (20) is rapidly varying. This allows us to use the method of stationary phase on the integral in Eq. (20). Doing so leads to evaluating the integral near the "stationary frequency",

$$\omega_s \doteq \frac{t}{\beta_2 z}, \tag{22}$$

and this gives the approximate solution

$$\begin{aligned} A_1(t,z) &\approx e^{-\frac{1}{2}i\Delta\beta_{\rm lin}z} e^{\gamma P_0 z} \hat{A}_1(\omega_s,0) e^{-\frac{it^2}{2\beta_2 z}} \\ &\quad \times \frac{1}{2\pi}\int e^{-\frac{2i}{\beta_2 z}(\omega'^2-\omega_s)^2}\, d\omega' \\ &\approx (1-i)(4\pi|\beta_2|z)^{-1/2} e^{-\frac{it^2}{2\beta_2 z}} e^{-\frac{1}{2}i\Delta\beta_{\rm lin}z} e^{\gamma P_0 z} \hat{A}_1(\omega_s,0). \end{aligned} \tag{23}$$

To see how the time-frequency relations arise from this solution, let us first assume that $\beta_2 > 0$. It follows from Eq. (23) that, in the time domain, the *temporal* output of "wave 1" has approximately the *same shape* as the input *spectrum*, but stretched out by the factor $\beta_2 z$ due to the denominator in the definition (22). Furthermore, because this system also exhibits SMI, the temporal output of "wave 2" has approximately the *reverse shape* of its stretched input spectrum. On the other hand, when $\beta_2 < 0$ (as in our computations in the picosecond and femtosecond regimes), these relations are reversed for the two waves. This explains the physical origin of the STSI feature in Fig. 1.

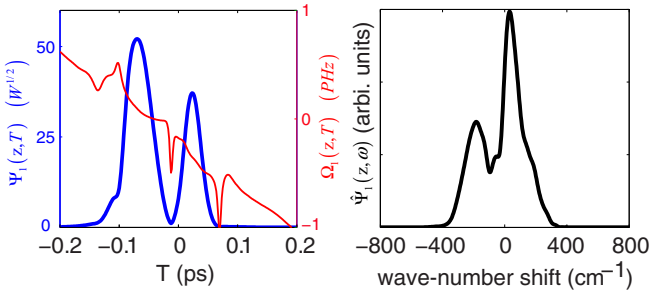

FIG. 10. (Color online) Spectral-temporal inversion for "wave 1" in the femtosecond regime.

To obtain further insight, we recall that the stationary phase approximation that leads to Eq. (23) depends on the pulse width being sufficiently short or, equivalently, the product of the GVD, and the propagation distance being sufficiently large. However, even when condition (21) is not satisfied, one can still make this approximation if there is a sufficiently strong initial chirp. In this case, we rewrite the input "wave 1" as

$$A_1(t,0) = e^{i\frac{Ct^2}{T^2}} f(t), \tag{24}$$

where C is chirp and $f(t)$ is a real-valued function. Therefore,

$$\hat{A}_1(\omega,0) = \frac{e^{-\frac{i}{4C}\omega^2}\hat{f}(\omega)}{\sqrt{1-\frac{2iC}{T^2}}}. \tag{25}$$

Using the transformation $\beta_2 z \to \beta_2 z + \frac{T^2}{2C}$, the above analysis is the same. In particular, condition (21) is replaced with

$$\left|\frac{\beta_2 z}{T^2} + \frac{1}{2C}\right| \gg 1 \tag{26}$$

and the chirp-shifted stationary frequency is

$$\omega_s \doteq \frac{t}{\beta_2 z + \frac{T^2}{2C}}. \tag{27}$$

Several important conclusions follow from (26) and (27).

(i) If $\beta_2 z + \frac{T^2}{2C} > 0$, the shape of $A_1(t,z)$ is a stretched-out version of its input spectrum, while the shape of $A_2(t,z)$ is reversed with respect to its stretched input spectrum; and *vice versa* if $\beta_2 z + \frac{T^2}{2C} < 0$.

(ii) If

$$\mathrm{sgn}C = \mathrm{sgn}\beta_2, \tag{28}$$

the chirp "helps" us observe the time-frequency duality relations, i.e., for larger C, condition (26) is satisfied at a shorter propagation time.

(iii) If

$$\mathrm{sgn}C = -\mathrm{sgn}\beta_2, \tag{29}$$

there is a "focal" propagation distance,

$$Z_C \approx \frac{\beta_2 T^2}{2C}, \tag{30}$$

at which there is a flip between the time-frequency relations of the two waves, i.e., the temporal and spectral shapes of one wave are the same for $z < Z_C$ and reversed for $z > Z_C$; and *vice versa* for the other wave.

We note that in order to obtain Eq. (25), the stationary phase approximation was made possible by adding a big initial chirp, even without making the assumption of ultrashort pulses and large GVD. In fact, the contribution from the GVD can be regarded as a "distributed chirp" that is applied during the pulse propagation, instead of an initial chirp at the input. Our previous computational results confirm this analysis. Specifically, in the femtosecond regime (Figs. 9 and 10), there is no need to chirp the input pulses due to the inherently large GVD. On the other hand, in the picosecond regime (Figs. 7 and 8), either chirping the input pulses or using large GVD waveguides is required. Interestingly, the requirement of having an input chip in the picosecond regime to observe STSI is exactly the same requirement for the distinguishable SMI

case, as discussed in Sec. IV A. Thus, SMI and STSI typically occur in tandem.

VI. SUMMARY AND CONCLUSIONS

In summary, we presented theoretical and computational studies on SMI and STSI. Starting from a nonlinear system of three coupled NLS-type equations, a simplified linear system of two coupled-wave equations was derived. Our analytic theory based on the special solutions of this simplified system captures the essential aspects of SMI and STSI. We also computationally demonstrate that the condition of energy conservation alone is not sufficient to deduce SMI. Our computational results for the nonlinear system show that only when the two waves are conjugated at the input will these two waves exhibit SMI features during pulses propagations. Furthermore, the combined effects of walk-off and chirp can either break SMI (when the inputs are not conjugated) or make it more visually distinguishable (when the inputs are conjugated). In addition, our study shows that SMI and STSI occur in tandem.

We note that the analysis is not limited to ultrashort pulses in the optical frequency regime, and the results of this study extend to wave dynamics in other nonlinear systems as well. These results shed light on the fundamental relationships between spectral and temporal properties of waves.

ACKNOWLEDGMENTS

We thank Kenneth K.Y. Wong, Carsten Langrock, and Kevin A. Mitchell for their comments. This work of C.G. and J.S. was supported by an AFOSR Young Investigator Award.

APPENDIX A: DERIVATION OF THE LINEAR SYSTEM (13) FROM THE NONLINEAR SYSTEM (8)

Here we derive the linear system (13) from the nonlinear system (8) under certain assumptions. First, we assume that the pump wave is much stronger than the sideband waves,

$$|A_p| \gg |A_1|, |A_2|. \tag{A1}$$

Second, we consider the usual experimental cases for a FWM process in which the wavelength of the pump is near the zero dispersion wavelength of the optical fiber [9]. In addition, if the difference between the wavelength of each sideband and the pump's wavelength is small, the variation of the GVD is approximately linear in this wavelength region (cf. [9]). These observations lead to the following three assumptions:

(i) The GVD experienced by the pump wave is negligible,

$$\beta_{2,p} \approx 0. \tag{A2}$$

(ii) The group velocities of the signal and idler waves are approximately the same,

$$\beta_{1,1} \approx \beta_{1,2}. \tag{A3}$$

(iii) The magnitudes of the GVDs of two waves are approximately the same, but their signs are opposite, $\beta_{2,1} = -\beta_{2,2} \equiv -\beta_2$.

Approximation (A3) implies that there is almost no relative walk-off between "wave 1" and "wave 2". For this reason, it is convenient to denote the *walk-off coefficient* as

$$\Delta\beta_1 \doteq \beta_{1,1} - \beta_{1,p}, \tag{A4}$$

which is between "wave n" and the pump wave.

Using (11) and (A1)–(A3), system (8) reduces to

$$i\frac{\partial A_p}{\partial z} + \gamma|A_p|^2 A_p = 0, \tag{A5a}$$

$$i\frac{\partial A_1}{\partial z} + i\Delta\beta_1\frac{\partial A_1}{\partial t} - \frac{1}{2}\beta_2\frac{\partial^2 A_1}{\partial t^2} + 2\gamma|A_p|^2 A_1 - \gamma A_p^2 A_2^* e^{-i\Delta\beta_{\rm lin} z} = 0, \tag{A5b}$$

$$i\frac{\partial A_2}{\partial z} + i\Delta\beta_1\frac{\partial A_2}{\partial t} + \frac{1}{2}\beta_2\frac{\partial^2 A_2}{\partial t^2} + 2\gamma|A_p|^2 A_2 - \gamma A_p^2 A_1^* e^{-i\Delta\beta_{\rm lin} z} = 0. \tag{A5c}$$

As with system (8), system (A5) is a coupled system of *nonlinear* equations, since A_p multiplies A_n. However, they can be further simplified as follows. Equation (A5a) can be solved in general as

$$A_p(t,z) = A_p(t,0)e^{i\gamma|A_p|^2 z}. \tag{A6}$$

Moreover, we assume that the temporal duration of the pump wave is much longer than that of the sideband waves. The latter implies that, for the propagation distances of interest, the pump wave can be regarded as a continuous wave rather than a pulse, i.e.,

$$A_p(t,z) \approx \sqrt{P_0}e^{i\gamma P_0 z}, \tag{A7}$$

where P_0 is the peak power of the input pump wave.

Substituting (A6) in (A5b) and (A5c) yields the *linearly coupled system* for the sideband waves,

$$i\frac{\partial A_1}{\partial z} + i\Delta\beta_1\frac{\partial A_1}{\partial t} - \frac{1}{2}\beta_2\frac{\partial^2 A_1}{\partial t^2} + 2\gamma P_0 A_1 - \gamma P_0 A_2^* e^{i(2\gamma P_0 - \Delta\beta_{\rm lin})z} = 0, \tag{A8a}$$

$$i\frac{\partial A_2}{\partial z} + i\Delta\beta_1\frac{\partial A_2}{\partial t} + \frac{1}{2}\beta_2\frac{\partial^2 A_2}{\partial t^2} + 2\gamma P_0 A_2 - \gamma P_0 A_1^* e^{i(2\gamma P_0 - \Delta\beta_{\rm lin})z} = 0. \tag{A8b}$$

System (A8) contains additional terms that are not present in system (13)—the second term corresponding to walk-off and the fourth term corresponding to XPM from the pump wave. These terms can be "removed" from the equations as follows. The second term is canceled by transforming to the moving coordinate frame,

$$\tilde{t} = t - (\Delta\beta_1)z.$$

The fourth term is canceled by rescaling the sideband fields as

$$A_n = \tilde{A}_n e^{-2i\gamma P_0 z}, \quad n = 1,2.$$

Doing so also partially cancels the phase $2i\gamma P_0$ in the fifth term. Thus, we achieve rescaled coupled equations as follows:

$$i\frac{\partial \tilde{A}_1}{\partial z} - \frac{1}{2}\beta_2\frac{\partial^2 \tilde{A}_1}{\partial \tilde{t}^2} - \gamma P_0 \tilde{A}_2^* e^{-i\Delta\beta_{\rm lin} z} = 0, \tag{A9a}$$

$$i\frac{\partial \tilde{A}_2}{\partial z} + \frac{1}{2}\beta_2\frac{\partial^2 \tilde{A}_2}{\partial \tilde{t}^2} - \gamma P_0 \tilde{A}_1^* e^{-i\Delta\beta_{\rm lin} z} = 0. \tag{A9b}$$

Removing all the tilde signs leads to system (13).

APPENDIX B: SOLUTION OF SYSTEM (13)

Taking the Fourier transform of system (13) gives

$$\frac{\partial \hat{A}_1(\omega,z)}{\partial z} - \frac{i}{2}\beta_2\omega^2\hat{A}_1(\omega,z) = -\frac{ie^{-i\Delta\beta_{\rm lin}z}}{L_{\rm nl}}\hat{A}_2^*(-\omega,z), \tag{B1a}$$

$$\frac{\partial \hat{A}_2(\omega,z)}{\partial z} + \frac{i}{2}\beta_2\omega^2\hat{A}_2(\omega,z) = -\frac{ie^{-i\Delta\beta_{\rm lin}z}}{L_{\rm nl}}\hat{A}_1^*(-\omega,z). \tag{B1b}$$

It is expedient to take the complex conjugate of (B1b) and make the transformation $\omega \to -\omega$. This gives

$$\frac{\partial \hat{A}_2^*(-\omega,z)}{\partial z} - \frac{i}{2}\beta_2\omega^2\hat{A}_2^*(-\omega,z) = \frac{ie^{-i\Delta\beta_{\rm lin}z}}{L_{\rm nl}}\hat{A}_1(\omega,z). \tag{B2}$$

Multiplying (B1a) and (B2) by the integrating factor

$$\mu(\omega,z) \doteq e^{-\frac{1}{2}i\beta_2\omega^2 z}$$

and rescaling the fields as

$$\hat{A}_n(\omega,z) = \frac{1}{\mu(\omega,z)}\hat{\mathcal{A}}_n(\omega,z), \quad n = 1,2 \tag{B3}$$

yields the system

$$\frac{\partial \hat{\mathcal{A}}_1(\omega,z)}{\partial z} = -\frac{ie^{-i\Delta\beta_{\rm lin}z}}{L_{\rm nl}}\hat{\mathcal{A}}_2^*(-\omega,z), \tag{B4a}$$

$$\frac{\partial \hat{\mathcal{A}}_2^*(-\omega,z)}{\partial z} = \frac{ie^{-i\Delta\beta_{\rm lin}z}}{L_{\rm nl}}\hat{\mathcal{A}}_1(\omega,z). \tag{B4b}$$

Taking the z derivative of (B4a) and substituting the right-hand side of (B4b) leads to a *second-order* linear equation for $\hat{\mathcal{A}}_1(\omega,z)$ as

$$\frac{\partial^2\hat{\mathcal{A}}_1}{\partial z^2} + i\Delta\beta_{\rm lin}\frac{\partial\hat{\mathcal{A}}_1}{\partial z} - \frac{1}{L_{\rm nl}^2}\hat{\mathcal{A}}_1 = 0. \tag{B5}$$

The characteristic equation obtained from the ansatz $\hat{\mathcal{A}}_1 = e^{rz/L_{\rm nl}}$ is

$$r^2 + i(L_{\rm nl}\Delta\beta_{\rm lin})r - 1 = 0.$$

The two solutions of this quadratic equation are

$$r_\pm = -\frac{iL_{\rm nl}\Delta\beta_{\rm lin}}{2} \pm \Gamma, \tag{B6}$$

where

$$\Gamma \doteq \sqrt{1 - \left(\frac{L_{\rm nl}\Delta\beta_{\rm lin}}{2}\right)^2} = \sqrt{1 - \left(\frac{\Delta\beta_{\rm lin}}{2\gamma P_0}\right)^2}. \tag{B7}$$

One can identify that $r_\pm$ is a normalized complex number, i.e.,

$$|r_\pm| = 1. \tag{B8}$$

In (B7), Γ is real-valued because of the relation $|\Delta\beta_{\rm lin}| < 2\gamma P_0$. This is due to our original assumption of a small difference between each sideband wavelength and the pump wavelength.

The general solution of (B5) is thus

$$\hat{\mathcal{A}}_1(\omega,z) = e^{-\frac{1}{2}i\Delta\beta_{\rm lin}z}[P_1(\omega)e^{\Gamma z/L_{\rm nl}} + Q_1(\omega)e^{-\Gamma z/L_{\rm nl}}],$$

where P_1 and Q_1 are arbitrary functions of frequency related to the input profiles (see below).

Using (B4a), the general solution for $\hat{\mathcal{A}}_2^*$ is

$$\hat{\mathcal{A}}_2^*(-\omega,z) = ie^{\frac{1}{2}i\Delta\beta_{\rm lin}z}[r_-P_1(\omega)e^{\Gamma z/L_{\rm nl}} - r_+Q_1(\omega)e^{-\Gamma z/L_{\rm nl}}].$$

Reverting to the unscaled fields using (B3), the general solution of system (13) is

$$\hat{A}_1(\omega,z) = e^{\frac{1}{2}i(\beta_2\omega^2-\Delta\beta_{\rm lin})z}[P_1(\omega)e^{\Gamma z/L_{\rm nl}} + Q_1(\omega)e^{-\Gamma z/L_{\rm nl}}], \tag{B9a}$$

$$\hat{A}_2(\omega,z) = -ie^{-\frac{1}{2}i(\beta_2\omega^2-\Delta\beta_{\rm lin})z}[r_-^*P_1(-\omega)e^{\Gamma z/L_{\rm nl}} - r_+^*Q_1(-\omega)e^{-\Gamma z/L_{\rm nl}}]. \tag{B9b}$$

The functions $P_1(\omega), Q_1(\omega)$ can be expressed in terms of the input spectral profiles as

$$P_1(\omega) = \frac{i}{L_{\rm nl}\Delta\beta_{\rm lin}}[r_-\hat{A}_1(\omega,0) + \hat{A}_2^*(-\omega,0)], \tag{B10a}$$

$$Q_1(\omega) = \frac{i}{L_{\rm nl}\Delta\beta_{\rm lin}}[r_-\hat{A}_1(\omega,0) - \hat{A}_2^*(-\omega,0)]. \tag{B10b}$$

To find special solutions with SMI features, by comparing (B9a) and (B9b) we identify that the two fields have the same type of exponential terms, but with linearly independent coefficients. Therefore, the two fields are proportional to each other if, and only if, either $Q_1(\omega) \equiv 0$ or $P_1(\omega) \equiv 0$.

One can identify that for the situation, either $Q_1(\omega) = 0$ or $P_1(\omega) = 0$ requires the initial condition of two inputs as

$$\hat{A}_2^*(-\omega,0) = \pm r_-\hat{A}_1(\omega,0). \tag{B11}$$

Choosing $Q_1(\omega) \equiv 0$ gives the relation

$$\hat{A}_2^*(-\omega,z) = ie^{\Delta\beta_{\rm lin}z}r_-\hat{A}_1(\omega,z), \tag{B12}$$

whereas, choosing $P_1(\omega) \equiv 0$ gives the relation

$$\hat{A}_2^*(-\omega,z) = -ie^{i\Delta\beta_{\rm lin}z}r_+\hat{A}_1(\omega,z), \tag{B13}$$

Taking the absolute values of either (B12) or (B13), we obtain the SMI relation (6). Note that it follows from (B12) and (B13) that each of these relations holds if, and only if, the input conjugated-wave condition Eq. (B11) is satisfied.

Furthermore, it is important to mention that system (13) has an asymptotic solution, which also exhibits SMI without the requirement of a conjugated wave as the input. Indeed, in (B9a) or (B9b) the terms with Q_1 are negligible for $z \to \infty$ as they are multiplied by decaying exponentials. Therefore, this analysis shows that SMI always hold for large propagation distances for system (13).

For completeness and the use in Sec. V, we explicitly state the SMI solution for the first wave when $Q_1(\omega) \equiv 0$,

$$\hat{A}_1(\omega,z) = e^{\frac{1}{2}i(\beta_2\omega^2-\Delta\beta_{\rm lin})z}e^{\gamma P_0\Gamma z}\hat{A}_1(\omega,0). \tag{B14}$$

[1] C. Gu, B. Ilan, and J. E. Sharping, Opt. Lett. **38**, 591 (2013).

[2] S. Watanabe, T. Naito, and T. Chikama, IEEE Photon. Technol. Lett. **5**, 92 (1993).

[3] A. H. Gnauck, R. M. Jopson, and R. M. Derosier, IEEE Photon. Technol. Lett. **5**, 663 (1993).
[4] R. Trebino, *Frequency-Resolved Optical Gating: The Measurement of Ultrashort Laser Pulses* (Kluwer, Boston, 2002).
[5] C. Iaconis and I. A. Walmsley, Opt. Lett. **23**, 792 (1998).
[6] K. Mori, T. Morioka, and M. Saruwatari, Opt. Lett. **21**, 110 (1996).
[7] K. Inoue, Opt. Lett. **22**, 1772 (1997).
[8] R. W. Boyd, *Nonlinear Optics* (Academic, New York, 2008).
[9] S. Wabnitz and J. M. Soto-Crespo, Opt. Lett. **23**, 265 (1998).
[10] G. P. Agrawal, *Nonlinear Fiber Optics* (Academic, New York, 2006).
[11] C. Gu, H. Wei, S. Chen, W. Tong, and J. E. Sharping, Opt. Lett. **35**, 351 (2010).
[12] C. Gu, C. Goulart, and J. E. Sharping, Opt. Lett. **36**, 1488 (2011).
[13] X. Xiao, P. Shum, E. S. Nazemosadat, and C. Yang, IEEE Photon. Technol. Lett. **20**, 1231 (2008).